Journal of Materials Chemistry A

PAPER

View Article Online
View Journal | View Issue

Cite this: J. Mater. Chem. A, 2015, 3, 12320

Unique synthesis of sandwiched graphene@($Li_{0.893}Fe_{0.036}$)$Co(PO_4)$ nanoparticles as high-performance cathode materials for lithium-ion batteries†

Li Liu,[a] Huijuan Zhang,[a] Xi Chen,[b] Ling Fang,[a] Yuanjuan Bai,[a] Ruchuan Liu[b] and Yu Wang*[a]

Received 20th March 2015
Accepted 25th April 2015

DOI: 10.1039/c5ta02058a

www.rsc.org/MaterialsA

In this report, a novel method towards synthesis of two-layer sandwiched graphene@($Li_{0.893}Fe_{0.036}$)$Co(PO_4)$ nanoparticles (SG@LFCPO) has been presented. In the approach, the sheet-like precursor, as the sacrificial template, and glucose molecules, as the carbon source, are the key factors involved in forming the specific morphology in which both top and bottom graphene sheets tightly envelop the ($Li_{0.893}Fe_{0.036}$)$Co(PO_4)$ nanoparticles, just like a sandwich. Owing to the combination of various favorable conditions, such as Fe doping, graphene coating and morphology design, the as-prepared SG@LFCPO displays very promising performance in terms of rate performance (discharge capacity of 85 mA h g^{-1} at 20 C), cyclability (coulombic efficiency of around 92.6%), stability (capacity retention of 94.6% after 100 cycles) and fast kinetics.

Introduction

In recent years, the range of applications of Li-ion batteries (LIBs) has been stretched from small-sized portable electronics to large-scale electric vehicles and stationary energy storage systems. Large-scale energy applications require the batteries to be economically efficient, highly safe, and to have high energy density and power density.[1] Therefore, high-energy, low-cost and long-life electrode materials are in urgent need to maintain the momentum of LIBs.[2] Among a variety of cathode materials, $LiCoO_2$ exhibits low structural and thermal stabilities,[3] leading to deficiencies for next generation applications entailing higher temperatures and more aggressive conditions, although it is the most widely used cathode in extant LIBs. Recently, there has been increasing interest in the use of lithium transition metal phosphates with olivine structure $LiMPO_4$ (M = Fe, Mn and Co) as potential cathode materials for LIBs.[2,4–6] The theoretical capacity of $LiMPO_4$ (170 mA h g^{-1}) provides higher energy density than that of $LiCoO_2$.[6,7] Besides, $LiMPO_4$ possesses strong P–O covalent bonds resulting in thermodynamical and dynamical stability at a high temperature and charge state.[8] Among the $LiMPO_4$ family, $LiFePO_4$ has been widely researched and commercially produced, owing to the eco-friendliness and thermal stability.[9–12] $LiMnPO_4$ is another promising cathode material with a higher operating voltage at ~4.1 V.[13,14] However, $LiFePO_4$ is limited by its low discharge potential (3.4 V *vs.* Li/Li^+) and $LiMnPO_4$ sustains Jahn–Teller distortion and large volume change during the charge–discharge cycles.[13,14] For these reasons, $LiCoPO_4$ has attracted plenty of attention even though Co is often considered an expensive element; in fact, $LiCoPO_4$ is expected to be cheaper than all commercialized LIBs in the market (due to the improved energy density).[15] $LiCoPO_4$ has advantages of flat high potential (at approximately 4.8 V *vs.* Li/Li^+), good theoretical capacity (167 mA h g^{-1}) and smaller structure volume change.[2,16] However, there are some drawbacks and unsolved problems for this high-voltage cathode material. The practical use of $LiCoPO_4$ is precluded by its poor rate cycling ability related to the inherently low electrical conductivity (<10^{-9} S cm^{-1}) and Li^+ ionic conductivity.[17,18] Besides, it suffers from capacity fade caused by structure deterioration and electrolyte decomposition.[19–21]

Consequently, many studies have focused on facilitating Li ionization and improving electrical conductivity, *e.g.*, doping metal ions, coating electrically conductive materials and shortening Li^+ diffusion paths.[22–25] While Cu, Cr, Mn, Al, Zr and Ni doping improves the electrochemical performance of $LiCoPO_4$,[22,26–31] doping-induced atomic-scale changes in structure and composition of $LiCoPO_4$ that lead to enhanced properties are yet to be revealed and fully exploited.[32] As we all know, Fe, as an environment friendly and low-price material, possesses an advantage of excellent electronic conductivity; thus doping $LiCoPO_4$ with Fe has been pursued to enhance

[a]The State Key Laboratory of Mechanical Transmissions and the School of Chemistry and Chemical Engineering, Chongqing University, 174 Shazheng Street, Shapingba District, Chongqing City, P. R. China, 400044. E-mail: wangy@cqu.edu.cn; prospectwy@gmail.com

[b]College of Physics, Chongqing University, No. 55 Daxuecheng South Rd, Shapingba, Chongqing, P. R. China

† Electronic supplementary information (ESI) available: See DOI: 10.1039/c5ta02058a

electronic conduction and bring the cost down. Meanwhile, coating $LiCoPO_4$ particles with conductive materials can improve electronic conductivity and protect particles from agglomeration at high synthesis temperature, desirable for facile lithium transport and better electrochemical properties.[33] From another point of view, down-sizing $LiCoPO_4$ has been shown to improve the electrochemical performance due to the shortening of Li^+ diffusion distance.[13,34]

In consideration of these reasons, a sandwich-like graphene-based composite, in which monodispersed nanoparticles are encapsulated in sandwiched graphene sheets, has been successfully fabricated. According to Prof. Wang *et al.*,[35] the unique morphology has a synergic effect on the electrochemical performance for LIB applications. In the synthesis process, a hydrated sheet-like precursor is prepared and submerged in 1 M $FeCl_2$ for 10 h. Then making use of the hydrogen-bond interaction, glucose molecules combine with the hydroxyls on the surface of sheet-like precursors to form the polymer-layers, which are graphitized into graphene sheets in sequence by calcinations in the argon atmosphere. In the meantime, the samples decompose and release CO_2, NH_3, and H_2O gas, forming the pores in the sandwiched structure. Following that, the precursors recrystallize into $(Li_{0.893}Fe_{0.036})Co(PO_4)$ nanoparticles. In the structure, the sandwiched graphene sheets tightly envelop the $(Li_{0.893}Fe_{0.036})Co(PO_4)$ nanoparticles to suppress the direct contact between electrolyte and active nanoparticles, decreasing the capacity loss. Obviously, Fe and graphene are favourable conductors; therefore the introduction of Fe and the formation of graphene could improve the electronic conductivity, speeding up the reaction kinetics. Furthermore, the pores in the novel structure might buffer the local volume change during the lithium insertion/extraction cycling, improving the structural stability of the electrode material. More importantly, the novel morphology with contractible active nanoparticles offers a shorter Li^+ diffusion pathway, enhancing the rate performance. To the best of our knowledge, these results first provide insights that pave the way for the rational design of two-layer sandwiched graphene@$(Li_{0.893}Fe_{0.036})Co(PO_4)$ nanoparticles as the cathode materials for LIBs and related applications.

Results and discussion

The fabrication process of the SG@LFCPO is schematically depicted in Scheme 1. The sheet-like precursors were first synthesized and submerged in 1 M $FeCl_2$ at room temperature for 10 h. Then the glucose molecules combined with the hydroxyls on the surface of the precursors by means of hydrogen-bonding interactions to form uniformly polymerized membranes, during the hydrothermal reaction. Following that, the solid-state reaction between the above obtained intermediate product and LiH_2PO_4 at the molar ratio of 1.1 : 1 was carried out at 720 °C in an Ar atmosphere. In the solid-state reaction, the polymerized films would be graphitized to form graphene sheets and the decomposable groups of the precursors would be decomposed to generate a mass of vacancies. Meanwhile, the precursors would shrink and aggregate,

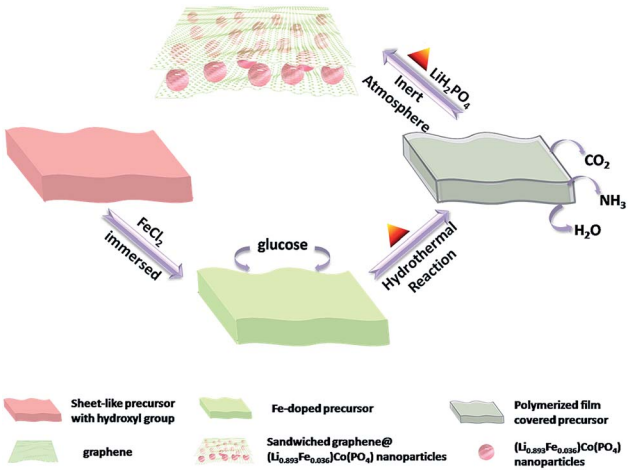

Scheme 1 Illustration of the preparation process of SG@LFCPO.

separately circling the individual crystallization centers to be recrystallized into nanoparticles, encapsulated by both top and bottom graphene sheets, on multiple sites.

The as-obtained SG@LFCPO and pristine $LiCoPO_4$ nanomesh were initially characterized by X-ray diffraction (XRD) to identify the crystallographic structure and crystallinity, shown in Fig. 1. The patterns can be assigned to the well-crystallized orthorhombic olivine structure of $(Li_{0.893}Fe_{0.036})Co(PO_4)$ (JCPDS no. 89-6193) and $LiCoPO_4$ (JCPDS no. 89-6192), respectively. No other peaks were observed for impurities. In the XRD pattern for the SG@LFCPO, the peak at 2θ of 31° (Co K_α) is seen, which represents the existence of graphene. Besides, the XRD pattern (Fig. S1 ESI†) reveals that the sheet-like precursor is highly crystalline. The crystal parameters of Fe-doped $LiCoPO_4$ and non-doped $LiCoPO_4$, calculated by Jade 5.0 software, are listed in Table 1. We find that for $(Li_{0.893}Fe_{0.036})Co(PO_4)$, the lattice parameter b is smaller than that of pure $LiCoPO_4$ while lattice parameters a and c increase slightly. For the reason that Li^+ diffusion energy is orientation-dependent which is the lowest for the pathway along the [010] channel, that is to say, along the b axis direction in the olivine structure,[36,37] as in the atomic

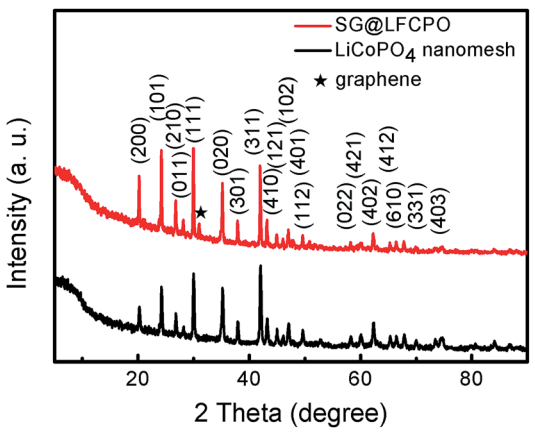

Fig. 1 XRD patterns for the SG@LFCPO and $LiCoPO_4$ nanomesh.

Table 1 Lattice constants for $(Li_{0.893}Fe_{0.036})Co(PO_4)$ and $LiCoPO_4$, calculated by Jade 5.0 software

	a (Å)	b (Å)	c (Å)
$LiCoPO_4$	10.20	5.92	4.700
$(Li_{0.893}Fe_{0.036})CoPO_4$	10.21	5.91	4.706

model shown in Fig. 2, the lattice parameters a and c increase slightly, suggesting that the Fe-doped $LiCoPO_4$ has a slightly wider Li^+ diffusion pathway. And, the lattice parameter b becomes smaller, demonstrating a shorter Li^+ diffusion pathway. All of these reveal that Fe doping is beneficial to fast Li^+ diffusion, which was also certified in the paper related to Na-doped $LiCoPO_4$.[38] Besides, we have recorded the Raman spectroscopy of SG@LFCPO, exhibited in Fig. S2.† The Raman bands at 1581.2 cm^{-1} (G band) arising from the first order scattering of the E_{2g} phonon of sp^2 C atoms, and 1328.3 cm^{-1} (D band) arising from a breathing mode of k-point photons of A_{1g} symmetry, are observed for SG@LFCPO, confirming the existence of graphene in the composite.

The morphology and thickness of as-obtained products were examined using scanning electron microscope (SEM) and atomic force microscope (AFM), respectively. By combining the SEM image (shown in Fig. 3a), the AFM image (Fig. S3a†) and the XRD pattern (Fig. S1†), we can see that the precursors possess a number of characteristics, such as high crystallinity (testified by the XRD pattern), 2-dimensional, ultrathin thickness down to ~10 nm (verified by the AFM image), uniform shape and large dimensions from several hundreds of square nanometers to tens of square micrometers (observed in the SEM image). As seen in Fig. 3b, the large scale samples have been obtained, illustrating that the method would be applied in large-scale commercial production. The SEM image in Fig. 3c displays that LFCPO nanoparticles homogeneously disperse in the double-layer sandwiched graphene sheets and separate from each other. Furthermore, according to Fig. 3c, the diameters of these LFCPO nanoparticles fall into a range of 40–80 nm. From the inset image in Fig. 3c, we know that the thickness of SG@LFCPO is estimated to be about 5–10 nm, in good agreement with the AFM image. Fig. S4a† shows the SEM image of pristine $LiCoPO_4$ nanomeshes, which is used for the contrast experiment. On account of the decomposition of the labile units, such as ammonium, hydrate and hydroxyl groups, a number of vacancies are formed for the pristine $LiCoPO_4$

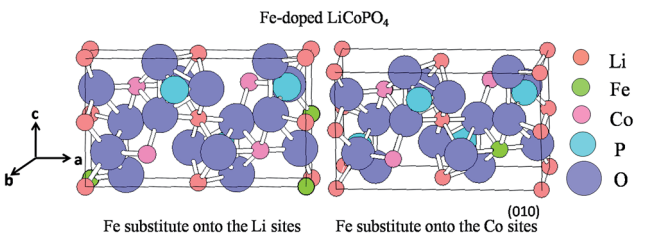

Fig. 2 The ball-and-stick model of Fe-doped $LiCoPO_4$ to illustrate the Li^+ diffusion pathway along the b axis direction.

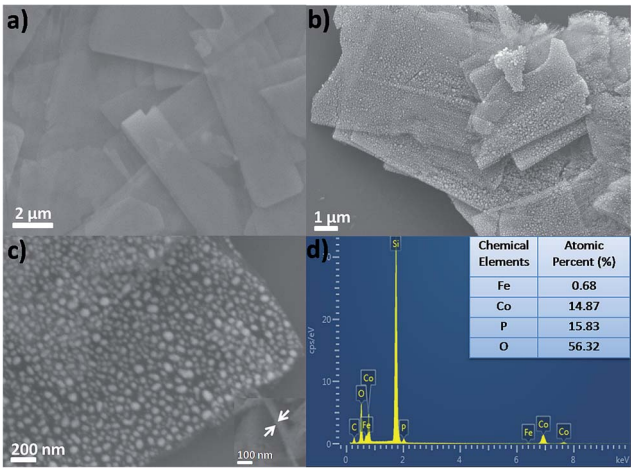

Fig. 3 (a) SEM image of $(NH_4)_2Co_8(CO_3)_6(OH)_6{\cdot}4H_2O$ sheet-like precursors; (b) SEM image of SG@LFCPO; (c) high-magnification SEM image of individual SG@LFCPO (the inset image is used to prove the thickness of SG@LFCPO); and (d) EDS image with the atomic percent data of SG@LFCPO.

nanomeshes. Fig. 3d displays the EDS spectra of the SG@LFCPO, which demonstrate that the composites contain C, Fe, Co, P and Si elements, wherein Si comes from the silicon substrates. Moreover, the Fe/Co ratio achieved from the EDS spectroscopy (Fig. 3d) is close to 1 : 0.04, in accordance with the XRD and XPS results. To further clarify the exact composition of the materials, the ICP-AES is conducted to obtain the elemental ratio of Li/Fe/Co, as shown in Table 2. As is expected, the results in Table 2 conform to those of EDS and XPS, illustrating effectively that the as-prepared material is the $(Li_{0.893}Fe_{0.036})Co(PO_4)$ phase with the exact composition. Furthermore the carbon content in the composite is about 7.6 wt% (see the Experimental section).

Transmission electron microscopy (TEM) is a powerful characterization tool to provide more insight into the composition and microstructure of the materials. The special morphology of the as-prepared SG@LFCPO is exhibited in Fig. 4a. Obviously, the LFCPO nanoparticles are monodispersed through the two-dimensional structure and do not stack to form an agglomerated structure on the supported graphene sheets, implying that the existence of double-layer graphene can prevent the nanoparticles from aggregating. According to the magnified TEM image, shown in Fig. 4b, the grain sizes of LFCPO nanoparticles are not different from those shown in Fig. 3c. The TEM image, in Fig. S4b,† indicates that a sheet-like precursor with regular morphology is ultrathin, which would be inherited from precursors to as-prepared SG@LFCPO. Fig. S4c† shows the TEM image of a pristine $LiCoPO_4$ nanomesh with a porous sheet-like structure. The high-resolution transmission electron microscope (HRTEM) image of SG@LFCPO, shown in Fig. 4c, verifies an individual LFCPO nanoparticle with a well-crystallized nature, as indicated by the white circles. The graphene is obviously observed outside the white circle, demonstrating that the graphene tightly parcels the active nanoparticles. Furthermore, along two mutually perpendicular

Table 2 Compositions of $LiCoPO_4$ and SG@LFCPO electrode materials, determined by ICP-AES

Composites	Targeted Li/Fe/Co ratio	Experimental (ICP-AES) Li/Fe/Co ratio
$LiCoPO_4$	1.00 : 0.00 : 1.00	0.99 : 0.001 : 1.003
SG@LFCPO	0.893 : 0.036 : 1.00	0.895 : 0.032 : 1.004

directions, there are fringes whose spacings are calculated to be 0.24 and 0.51 nm, corresponding to (002) and (200) crystal planes in orthorhombic $(Li_{0.893}Fe_{0.036})Co(PO_4)$, respectively. The results show that the thinnest part of the SG@LFCPO is along the *b*-axis, which is the favorable direction for the Li^+ diffusion. According to the AFM image, in Fig. S3b,† the thickness of SG@LFCPO is estimated to be ~10 nm, which reveals a short Li^+ diffusion pathway and a fast Li^+ diffusion kinetics. The Brunauer–Emmett–Teller (BET) measurement was performed to determine the surface area and pore size distribution of SG@LFCPO and pristine $LiCoPO_4$ nanomesh, respectively. Fig. 4d reveals that the surface area of SG@LFCPO is up to 280.6 $m^2\ g^{-1}$; meanwhile, the pore size is centered at around 4.85 nm (inset of Fig. 4d). However, the specific surface area of 52.57 $m^2\ g^{-1}$ is achieved for a pristine $LiCoPO_4$ nanomesh, according to Fig. S4d,† and the pore size is mainly distributed around 6.12 nm. Therefore, it can be seen that designing a novel morphology could increase the specific surface area and voidage, facilitating the transmission of the electrolyte. The elemental mappings of the SG@LFCPO based on Fig. S5a† are displayed in Fig. S5b–S5f,† from which it can be observed that C, O, Co, Fe and P elements are homogeneously distributed. The above results suggest that the SG@LFCPO would exhibit a good electrochemical performance with electrolyte flooding and Li^+ diffusion.

In order to confirm the valence states of the elements present in the $(Li_{0.893}Fe_{0.036})Co(PO_4)$ composite, X-ray photoelectron spectroscopy (XPS) measurement was carried out, and the corresponding spectra are displayed in Fig. S6† after calibration by the standard XPS peak of C1s. The observed C1s peak at 284.8 eV mainly represents graphitic carbon.[39] The peak binding energy at 532.8 eV, in Fig. S6b,† is attributed to O1s of P–O–P bonds.[40] Besides, the P2p band is observed at 133.8 eV for $P2p_{3/2}$, which is consistent with the value reported for P^{5+} in PO_4.[41] Fig. S6d and S6e† clearly show the presence of Fe2p and Co3p core levels with no trace of impurities. The core level photoelectron peaks at 710.8 eV are well assigned to $Fe2p_{3/2}$, suggesting that Fe is in its divalent state in agreement with previous works.[42] In addition, the Co3p level is observed at 60.8 eV for $Co3p_{3/2}$, which may be due to spin orbital interactions, indicating the presence of Co^{2+}.[43]

The electrochemical performance of SG@LFCPO is investigated using a Li metal as the anode at various current densities between 2.5 and 4.95 V *vs.* Li/Li^+. The typical charge–discharge curves of the SG@LFCPO for different cycles at a 0.1 C rate are displayed in Fig. 5a. The discharge curves showing only one

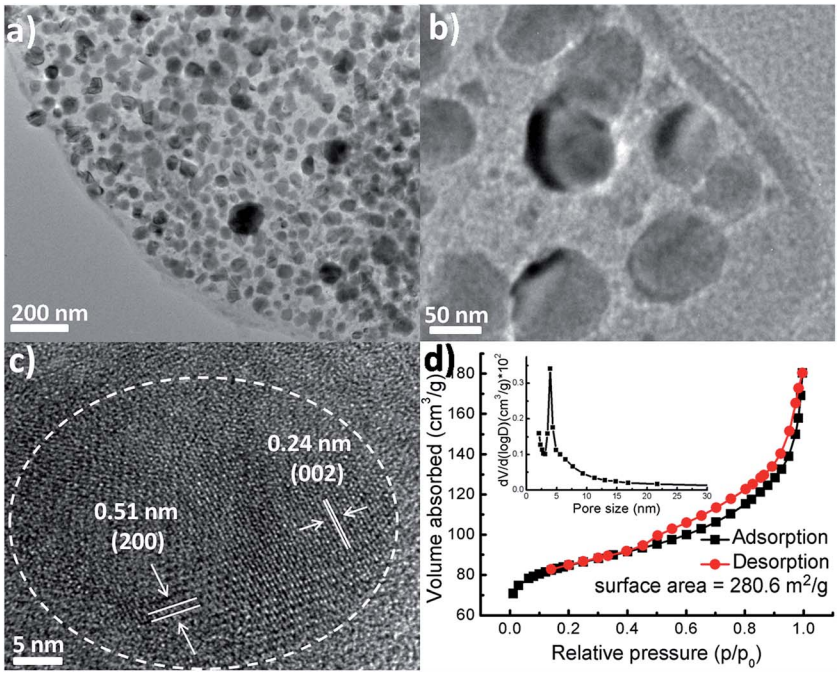

Fig. 4 (a and b) Stepwise magnified TEM images of SG@LFCPO; (c) the locally magnified HRTEM image of SG@LFCPO; and (d) nitrogen adsorption–desorption isotherm and the corresponding pore size distribution (inset) of SG@LFCPO.

plateau can be supported by the one-step mechanism of lithium deintercalation.[44] All the discharge curves exhibit a wide and flat voltage plateau at approximately 4.72 V, implying that the electrode structure is stable in the voltage range. In the initial charging–discharging cycle, the reaction between the active material of the electrode and the electrolyte leads to the decomposition of the electrolyte and the formation of an SEI film on the electrode, causing the initial discharge capacity to be much less than the charge capacity. From the second cycle, however, the discharge capacity loss is gradually diminished. The discharge capacities are approximately 150, 148, 147 and 142 mA h g^{-1} at the 2nd, 10th, 50th and 100th cycles, respectively, demonstrating the outstanding capacity retention of 94.6% for SG@LFCPO. However, when it comes to the charge–discharge curves of the pristine $LiCoPO_4$ nanomesh in Fig. 5b, we can see a fast recession of discharge capacity in the wake of the incremental cycle-index. The contrast of Fig. 5a and b indicates that coating graphene and doping Fe are in favour of the structure stability. Of course, the cyclic voltammetry (CV) measurement is adopted to investigate the electrochemical characteristics, as shown in Fig. S7a.† The oxidation peak and reduction peak at ~4.72 and ~4.66 V, respectively, are attributed to the redox reaction of Co^{2+}/Co^{3+}, in accordance with the results of charge–discharge curves. Besides, it can be seen that except for the first cycle, the curves in the subsequent cycles follow almost the same path, indicating high stability and reversibility for Li^+ insertion and extraction. And the potential difference between the two peaks is less than 0.1 V, suggesting an excellent rate performance. Because of the importance of evaluating total performance, the rate performance of SG@LFCPO and pristine $LiCoPO_4$ nanomesh is researched in Fig. 5c. The cells were first cycled at 0.1 C for 10 cycles, followed by cycling with a stepwise increase of the discharge current densities to as high as 20 C. An average discharge capacity of 85 mA h g^{-1} was obtained at the highest current density of 20 C, and conversely, the rest of discharge capacity is a little for the pristine $LiCoPO_4$ nanomesh. Moreover, at the rates of 0.1, 1, 5 and 10 C, the corresponding discharge capacities were 150, 145, 129 and 104 mA h g^{-1} for SG@LFCPO, *versus* 118, 93, 67 and 35 mA h g^{-1} for the pristine $LiCoPO_4$ nanomesh. When the discharge rate was changed back to 0.1 C after the high-rate charge–discharge cycling, the reversible discharge capacity of SG@LFCPO returned to 148 mA h g^{-1}. Obviously, the SG@LFCPO reveals much better rate performance than the pristine $LiCoPO_4$ counterpart. The galvanostatic measurement at a rate of 0.1 C is shown in Fig. 5d to present the coulombic efficiency, cyclability and specific capacity upon 100 cycles. It is easy to discover that the charge and discharge capacities slightly descend after 100 cycles. Except the initial cycle, the charge capacity and discharge capacity of SG@LFCPO can be retained at ~162 and 150 mA h g^{-1}, respectively, with a high coulombic efficiency of around 92.6%. Interestingly, the coulombic efficiencies of the first several cycles are relatively lower than those of the subsequent cycles. The possible reason is that the active materials could not completely make contact with the electrolyte in the first several cycles, causing the capacity to decrease. As the redox reaction proceeds, the electrolyte penetrates into the inner part of the void space, resulting in the increased capacities. However, as shown in Fig. S7b,† the discharge capacity of the pristine $LiCoPO_4$ nanomesh declines to 52 mA h g^{-1} and the capacity retention is 56.7% after 100 cycles, which are tremendously inferior to those of SG@LFCPO. Fig. S8† shows the SEM image of SG@LFCPO after electrochemical testing. As shown in Fig. S8,† although the aggregation of the SG@LFCPO after electrochemical testing is observed, the structure of two-layer sandwiched graphene@$(Li_{0.893}Fe_{0.036})Co(PO_4)$ nanoparticles is

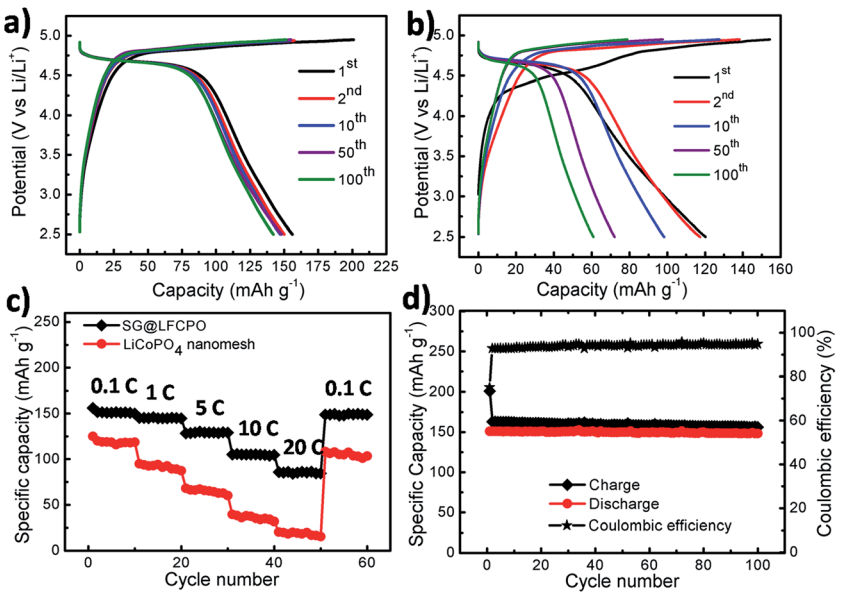

Fig. 5 Galvanostatic discharge and charge curves in the voltage range of 2.5–4.95 V *vs.* Li at 0.1 C of (a) SG@LFCPO; (b) $LiCoPO_4$ nanomesh; (c) the rate performance at different discharge rates, 0.1, 1, 5, 10 and 20 C, respectively, in the voltage range between 2.5 and 4.95 V of SG@LFCPO and $LiCoPO_4$ nanomesh; and (d) the charge–discharge capacities and corresponding coulombic efficiency of SG@LFCPO.

retained, further supporting the claims of the excellent stability and cyclability. Owing to the fact that operating temperature is also a determiner of cell performance, herein, the temperature-dependent Li storage and rate performance of the SG@LFCPO have been studied, shown in Fig. S7c and S7d.† At the testing temperature of 50 °C, the delivered capacity at a rate of 0.1 C is the highest, while the cycling stability is the worst. The reason is that the activation of electrode materials could be accelerated by the high temperature, in favour of the discharge capacity. In contrast, the high temperature could accelerate the severe decomposition of the electrolyte to release some gas, such as HF, PF_5, *etc.*, leading to the increase in internal pressure and deformation of the battery. Thus the cyclability at 50 °C is inferior to that at 25 and 0 °C; however, the rate performance gradually increases with the testing temperature varying from 0, 25 to 50 °C. The electrochemical impedance spectroscope (EIS) data of SG@LFCPO and $LiCoPO_4$ nanomesh are shown in Fig. S9.† The impedance spectra for both samples show a single semi-circle at higher frequency followed by a straight line at a slope of approximately 45° at lower frequency. The semi-circle at higher frequency is assigned to the charge transfer resistance (R_{ct}), related to the electrochemical reaction. It can be seen that formation of graphene encapsulating outside and the introduction of Fe into $LiCoPO_4$ could remarkably reduce the value of R_{ct}, indicating an enhancement in the kinetics and the consequent improvement in high-rate capabilities.

These results herein give clear evidence that compared with the pristine $LiCoPO_4$ nanomesh, SG@LFCPO possesses preferable electrochemical performance, for instance superior rate performance, outstanding cyclability, admirable stability and fast kinetics of extraction/insertion Li^+. The improvements arise from three major factors, which are Fe doping, coating graphene and designing the novel morphology. In the first place, Fe, as an excellent conductive material, could compensate the poor electronic conductivity of $LiCoPO_4$. Besides, the lattice parameter *a* slightly increases and *b* tinily diminishes after Fe doping, resulting in a shorter and wider Li^+ diffusion pathway. As we all know, the operating voltage of $LiCoPO_4$ is very high; however, the electrolyte gets easily decomposed at high voltage. This problem can be solved by coating graphene to reduce the direct contact between electrolyte and active material, enhancing the capacity retention. On the other hand, designing the porous morphology in which sandwiched graphene sheets tightly envelop functional nanoparticles could shorten the Li^+ diffusion channel. In addition, the existence of void space could buffer the volume changes during the insertion/extraction of Li^+, improving the cyclability of the cathode material.

Conclusion

In this work, two-layer sandwiched graphene@($Li_{0.893}Fe_{0.036}$)$Co(PO_4)$ nanoparticles have been successfully fabricated through the template-sacrificial method. The sheet-like precursors, as the template, and glucose molecules, as the carbon source, are the key factors involved in the synthesis process, contributing to the novel morphology in which the LFCPO nanoparticles are tightly enveloped by the sandwiched graphene sheets. The as-prepared SG@LFCPO, with an ultra-thin thickness of approximately 10 nm and the surface area of 280.6 $m^2\ g^{-1}$, display very promising performance in terms of rate performance (discharge capacity of 85 mA h g^{-1} at 20 C), cyclability (coulombic efficiency of around 92.6%), stability (capacity retention of 94.6% after 100 cycles) and fast kinetics due to the combination of various favorable conditions. Undoubtedly, our research provides key insights that pave the way for the rational design and realization of graphene-based materials for LIBs and related applications.

Experimental section

Materials

All chemicals or materials were utilized directly without any further purification before use: ethylene glycol (Fisher Chemical, 99.99%), ammonium hydroxide ($NH_3 \cdot H_2O$, 28–30 wt%, J. T. Baker), cobalt nitrate ($Co(NO_3)_2 \cdot 6H_2O$, 99.9%, Aldrich), sodium carbonate (Na_2CO_3, 99.9%, Aldrich), ferrous chloride ($FeCl_2$, 99.9%, Aldrich), lithium dihydrogen phosphate (LiH_2PO_4, 99.9%, Aldrich) and anhydrous ethanol (Fisher Chemical, 99.99%).

Preparation of $(NH_4)_2Co_8(CO_3)_6(OH)_6 \cdot 4H_2O$ nanosheets

$(NH_4)_2Co_8(CO_3)_6(OH)_6 \cdot 4H_2O$ nanosheets were synthesized by a hydrothermal reaction. Ethylene glycol (12.5 mL), concentrated $NH_3 \cdot H_2O$ (12.5 mL), 1 M Na_2CO_3 aqueous solution (5 mL), and 1 M $Co(NO_3)_2$ aqueous solution (5 mL) were mixed step-by-step under strong stirring at intervals of 1–2 min. After that, the precursor solution was stirred for another 20 min. Then, the mixture changed into a deep pink-violet homogeneous solution. Once the mixture solution was transferred into a Teflon-lined stainless steel autoclave with a volume of 45 mL, a thermal treatment was performed for the Teflon-liner in an electric oven at 170 °C for 17 h. After the autoclave was cooled down naturally to room temperature in air, samples deposited at the bottom were collected and washed by centrifugation for at least three cycles using deionized water (D.I. water) and two cycles using anhydrous ethanol. Finally, the as-synthesized samples were dried in a vacuum oven at 60 °C overnight to remove the absorbed water for the subsequent fabrications and characterizations.

Preparation of SG@LFCPO and the $LiCoPO_4$ nanomesh

$(NH_4)_2Co_8(CO_3)_6(OH)_6 \cdot 4H_2O$ nanosheets (100 mg) were immersed in a 1 M $FeCl_2$ aqueous solution for 10 h. Then, the samples were centrifuged, repeating the same steps. Following that, the as-synthesized samples were dried in a vacuum oven at 60 °C overnight. Fe-doped $(NH_4)_2Co_8(CO_3)_6(OH)_6 \cdot 4H_2O$ nanosheets (100 mg) were ultrasonically mixed with glucose aqueous solution (5 mL 1 M) together with additional deionized water (25 mL) to form a homogeneous solution. The above mixed solution was poured into a 45 mL Teflon-lined stainless steel autoclave and sealed tightly. Next, the liner was heated in an electric oven at 180 °C for 8 h. After that, the sample was washed using centrifugation by the same method, and then dried at

60 °C overnight. Then, the above samples were converted to the SG@LFCPO when they (130.18 mg) reacted with LiH_2PO_4 (114.32 mg) at 720 °C under an Ar atmosphere in the tube furnace. For the synthesis of a $LiCoPO_4$ nanomesh, the experimental procedures followed the same processes as the SG@LFCPO except for immersion in a $FeCl_2$ solution and hydrothermal reaction with a glucose aqueous solution.

Characterization of the samples

Field-emission SEM (JEOL JSM-7800F) coupled with an EDS analyzer (JEOL, JSM-7800F), TEM coupled with an EDX analyzer (Philips, Tecnai, F30, 300 kV), X-ray photoelectron spectrometry with an ESCALAB250 analyzer (XPS), powder X-ray diffraction (Bruker D8 Advance X-ray diffractometer with Co K_α radiation (λ = 1.78897 Å)), Brunauer–Emmett–Teller surface area measurement (BET, Quantachrome Autosorb-6B surface area and pore size analyzer), Raman spectroscopy (RENISHAW Invia Raman Microscope, voltage (AC) 100–240 V, power 150 W), and Atomic Force Microscope (AFM, Asylum Research, MFP-3D) were used to characterize the obtained samples. The elementary compositions of the materials were determined by inductively coupled plasma-atomic emission spectroscopy (ICP-AES, iCAP 6300 Duo).

Carbon content tests

Firstly, 200.00 mg of the samples (SG@LFCPO) were added in concentrated hydrochloric acid. After 24 hours' stirring, the $(Li_{0.893}Fe_{0.036})Co(PO_4)$ nanoparticles were completely dissolved in the acid. Then the undissolved carbon was collected and washed with deionized water and anhydrous ethanol. Following that, the carbon was dried in an oven at 60 °C overnight to remove absorbed water and ethanol. The carbon weight measurements were taken using a Mettler-Toledo analytical balance. The carbon content of SG@LFCPO was then calculated using the formula:

$$C\% = W(C)/W(SG@LFCPO) \times 100\%$$

where W(C) and W(SG@LFCPO) were the weight of carbon and SG@LFCPO, respectively. The results show that the carbon content in the as-prepared material is approximately 7.6 wt% by calculation. For comparison, $(Li_{0.893}Fe_{0.036})Co(PO_4)$ particles (200 mg) without carbon coating were synthesized and dissolved in concentrated hydrochloric acid by the same process.

Electrochemical testing

A homogeneous mixture composed of the SG@LFCPO, carbon black, and polyvinyl difluoride (PVDF) using 1-methyl-2-pyrrolidinone (NMP) as the solvent at a weight ratio of 80 : 15 : 5 was prepared under strong magnetic stirring for at least 1 day. Then some of the mixture was extracted and spread onto Al foils. Before and after the samples were spread, the Al foils were weighed using a high-precision analytical balance. The read difference was the exact mass of the coated samples on Al foils. Normally, the sample loadings range from 1.2 to 1.6 mg cm^{-2}. The obtained pieces of Al covered with samples were then used as working electrodes with 1 M $LiPF_6$ in ethylene carbonate and diethyl carbonate (EC/DMC = 1 : 1 v/v) as the electrolyte. Celgard 2400 was applied as the separator film to isolate the two electrodes. Pure Li foil (99.9%, Aldrich) served as the counter electrode and reference electrode. The cell was assembled in an argon filled glove box in which moisture and oxygen concentrations were strictly limited to below 0.1 ppm. The galvanostatic cycling was performed using a Neware battery testing system (model 5 V 5 mA), and CV data were recorded at a scanning rate of 0.1 mV s^{-1} between 2.5 and 4.95 V using an Autolab (model AUT71740) in a three-electrode cell. For the electrochemical impedance spectroscopy (EIS) measurements, the open circuit potential (OCP) was determined first and then the AC potential was set at ±10 mV (rms) around the OCP. A frequency range of 0.01 Hz to 100 Hz was used by the CHI604E electrochemical analyzer to ensure good data quality for subsequent model fitting. Then, the data acquired from the impedance testing were analyzed using Zview Version 3.2c-software.

Acknowledgements

This work was financially supported by the Thousand Young Talents Program of the Chinese Central Government (Grant no. 0220002102003), National Natural Science Foundation of China (NSFC, Grant no. 21373280 and 21403019), Beijing National Laboratory for Molecular Sciences (BNLMS), the Fundamental Research Funds for the Central Universities (106112015CDJZR285519) and Hundred Talents Program at Chongqing University (Grant no. 0903005203205).

References and notes

1 N. R. Khasanova, O. A. Drozhzhin, S. S. Fedotov, D. A. Storozhilova, R. V. Panin and E. V. Antipov, *Beilstein J. Nanotechnol.*, 2013, **4**, 860–867.
2 K. Amine, H. Yasuda and M. Yamachi, *Electrochem. Solid-State Lett.*, 2000, **3**, 178–179.
3 M. S. Whittingham, *Chem. Rev.*, 2004, **104**, 4271–4301.
4 A. K. Padhi, K. S. Nanjundaswamy and J. B. Goodenough, *J. Electrochem. Soc.*, 1997, **144**, 1188–1194.
5 J. Carrasco, N. Lopez and F. Illas, *Phys. Rev. Lett.*, 2004, **93**, 225502–225505.
6 A. Yamada and S.-C. Chung, *J. Electrochem. Soc.*, 2001, **148**, A960–A967.
7 K.-F. Hsu, S.-Y. Tsay and B.-J. Hwang, *J. Mater. Chem.*, 2004, **14**, 2690–2695.
8 Q. D. Truong, M. K. Devaraju, Y. Ganbe, T. Tomai and I. Honma, *Sci. Rep.*, 2014, **4**, 3975.
9 C. Delmas, M. Maccario, L. Croguennec, F. Le Cras and F. Weill, *Nat. Mater.*, 2008, **7**, 665–671.
10 S. W. Oh, S.-T. Myung, S.-M. Oh, K. H. Oh, K. Amine, B. Scrosati and Y.-K. Sun, *Adv. Mater.*, 2010, **22**, 4842–4845.
11 W.-J. Zhang, *J. Electrochem. Soc.*, 2010, **157**, A1040–A1046.
12 B. Kang and G. Ceder, *Nature*, 2009, **458**, 190–193.
13 T. N. L. Doan and I. Taniguchi, *J. Power Sources*, 2011, **196**, 1399–1408.

14 D. Rangappa, K. Sone, Y. Zhou, T. Kudo and I. Honma, *J. Mater. Chem.*, 2011, **21**, 15813–15818.
15 J. L. Allen, J. L. Allen, S. A. Delp and T. R. Jow, *ECS Trans.*, 2014, **61**, 63–68.
16 S. Okada, S. Sawa, Y. Uebou, M. Egashira, J. Yamaki, M. Tabuchi, H. Kobayashi, K. Fukumi and H. Kageyama, *Electrochemistry*, 2003, **71**, 1136–1138.
17 A. Yamada, H. Koizumi, S. I. Nishimura, N. Sonoyama, R. Kanno, M. Yonemura, T. Nakamura and Y. Kobayashi, *Nat. Mater.*, 2006, **5**, 357–360.
18 J. Wolfenstine, B. Poese and J. L. Allen, *J. Power Sources*, 2004, **138**, 281–282.
19 K. Tadanaga, F. Mizuno, A. Hayashi, T. Minami and M. Tatsumisago, *Electrochemistry*, 2003, **71**, 1192–1195.
20 N. N. Bramnik, K. G. Bramnik, C. Baehtz and H. Ehrenberg, *J. Power Sources*, 2005, **145**, 74–81.
21 J. Wolfenstine, U. Lee, B. Poese and J. L. Allen, *J. Power Sources*, 2005, **144**, 226–230.
22 M. V. V. M. S. Kishore and U. V. Varadaraju, *Mater. Res. Bull.*, 2005, **40**, 1705–1712.
23 J. Wolfenstine, J. Read and J. L. Allen, *J. Power Sources*, 2007, **163**, 1070–1073.
24 Y. Hu, M. M. Doeff, R. Kostecki and R. Fiñones, *J. Electrochem. Soc.*, 2004, **151**, A1279–A1285.
25 D. Wang, H. Li, S. Shi, X. Huang and L. Chen, *Electrochim. Acta*, 2005, **50**, 2955–2958.
26 J. Wolfenstine, *J. Power Sources*, 2006, **158**, 1431–1435.
27 S.-Y. Chung, J. T. Bloking and Y.-M. Chiang, *Nat. Mater.*, 2002, **1**, 123–128.
28 J. L. Allen, T. R. Jow and J. Wolfenstine, *J. Power Sources*, 2011, **196**, 8656–8661.
29 D.-W. Han, Y.-M. Kang, R.-Z. Yin, M.-S. Song and H.-S. Kwon, *Electrochem. Commun.*, 2009, **11**, 137–140.
30 I. Taniguchi, T. N. L. Doan and B. Shao, *Electrochim. Acta*, 2011, **56**, 7680–7685.
31 J. Wolfenstine and J. Allen, *J. Power Sources*, 2004, **136**, 150–153.
32 Z. P. Lin, Y. J. Zhao and Y. M. Zhao, *Chin. Phys. Lett.*, 2009, **26**, 038202.
33 D. Bhuvaneswari, Gangulibabu, C. H. Doh and N. Kalaiselvi, *Int. J. Electrochem. Sci.*, 2011, **6**, 3714–3728.
34 J. Liu, T. E. Conry, X. Song, L. Yang, M. M. Doeff and T. J. Richardson, *J. Mater. Chem.*, 2011, **21**, 9984–9987.
35 H. J. Zhang, Y. J. Bai, Y. Y. Feng, X. Li and Y. Wang, *Nanoscale*, 2013, **5**, 2243–2248.
36 D. Morgan, A. Van der Ven and G. Ceder, *Electrochem. Solid-State Lett.*, 2004, **7**, A30–A32.
37 G. Chen, X. Song and T. J. Richardson, *Electrochem. Solid-State Lett.*, 2006, **9**, A295–A298.
38 Z. P. Lin, Y. J. Zhao and Y. M. Zhao, *Chin. Phys. Lett.*, 2009, **26**, 038202.
39 X. Zhou, F. Wang, Y. Zhu and Z. Liu, *J. Mater. Chem.*, 2011, **21**, 3353–3358.
40 P. Y. Shih, S. W. Yung and T. S. Chin, *J. Non-Cryst. Solids*, 1998, **224**, 143–152.
41 Y. J. Park, Y.-S. Hong, X. Wu, K. S. Ryu and S. H. Chang, *J. Power Sources*, 2004, **129**, 288–295.
42 V. Di Castro and S. Ciampi, *Surf. Sci.*, 1995, **331–333**, 294–299.
43 N. S. McIntyre and M. G. Cook, *Anal. Chem.*, 1975, **47**, 2208–2213.
44 N. Bramnik, K. Bramnik, T. Buhrmester, C. Baehtz, H. Ehrenberg and H. Fuess, *J. Solid State Electrochem.*, 2004, **8**, 558–564.